# LA-UR-22-27950

**Approved for public release; distribution is unlimited.**

| | |
|---|---|
| **Title:** | Development of a creep model informed by lower-length scale simulations to simulate creep in doped UO2 |
| **Author(s):** | Galvin, Conor Oscar<br>Chakraborty, Aritra<br>Andersson, Anders David Ragnar<br>Capolungo, Laurent<br>Cooper, Michael William Donald |
| **Intended for:** | Report |
| **Issued:** | 2023-03-15 (rev.1) |



Los Alamos
NATIONAL LABORATORY

# Development of a creep model informed by lower-length scale simulations to simulate creep in doped $UO_2$

C. O. T. Galvin, A. Chakraborty, D. A. Andersson, L. Capolungo, and M. W. D. Cooper

*Materials Science and Technology Division, Los Alamos National Laboratory*

August 01$^{st}$, 2022

# Executive Summary

Using molecular dynamics, we predict information at the atomistic scale used to develop a mechanistic $UO_2$ creep model for use in higher length-scale fuel performance codes. The ultimate objective of the model is to better describe the grain size dependence and therefore impact of doping on creep rates in $UO_2$. In a previous NEAMS milestone, we found that Nabarro-Herring (bulk diffusional) creep was too low to capture the experimentally observed creep rates in standard $UO_2$. Moreover, in that milestone, other mechanisms were explored, such as Coble (grain boundary) creep and dislocation climb, with each mechanism exhibiting different grain size dependencies. Again, these were orders of magnitude too low to describe the experimental creep rates.

In this work, we address the previous assumptions made for the Coble creep mechanism by investigating the diffusivity of various defects at grain boundaries in $UO_2$ and, critically, to determine if enhanced grain boundary diffusivity allows the model to better reproduce experimental results. The diffusivity as a function of temperature for different concentrations of uranium vacancies and interstitials for bulk $UO_2$ have also been examined using cluster dynamics. Furthermore, using a concentration dependent segregation model, the concentration of defects at the grain boundary were predicted. This atomistic data was then input into the various creep mechanisms and the creep rates compared to the empirical MATPRO correlation (used in BISON) and experiment.

The application of these atomic scale data within a polycrystal constitutive plasticity model was also demonstrated. From this it was shown the importance of the GB diffusional creep mechanism to overall creep rates. This is a significant step in the use of lower length scale atomistic data capturing the mechanistic behaviour used in the development of a polycrystal plasticity model that can describe $UO_2$ deformation for in-reactor conditions. Once validated for standard $UO_2$, the model will be used to inform a diffusion mediated creep model applied to doped $UO_2$.

# Glossary

**BISON** Finite element-based nuclear fuel performance code
**GB** Grain Boundary
**LWR** Light water reactor
**MD** Molecular dynamics
**MSD** Mean squared displacement
$\mathbf{E_{mig}}$ Migration energy
$\mathbf{D_x}$ Diffusion coefficient of a defect, **x**
$\mathbf{D_{V_U}}$ Diffusion coefficient of uranium vacancy
$\mathbf{D_{U_i}}$ Diffusion coefficient of uranium interstitial
$\mathbf{D_{V_U}^{GB}}$ Diffusion coefficient of uranium vacancy at a grain boundary
$\mathbf{D_{U_i}^{GB}}$ Diffusion coefficient of uranium interstitial at a grain boundary
$\mathbf{D_0}$ Diffusion pre-exponential
$\mathbf{D_{0_{Self}}}$ Self-diffusion pre-exponential
$\mathbf{D_{Self}}$ Self-diffusion coefficient ($\mathbf{D_x}$multiplied by concentration of **x**)

# Contents

# List of Figures

# 1 Introduction

Uranium dioxide ($UO_2$) is the most common fuel type used in commercial light water reactors (LWRs) due to its suitable material properties and the benefit of years of operational experience. Additionally, $UO_2$ material properties make it suitable for LWR operation, such as a high melting point, radiation tolerance, chemical stability and accomodation of non-stoichiometry and fission products. Advanced fuels are currently being developed for use in LWRs to potentially provide better fuel performance and economics of operation. One of these advanced fuel candidates is doped $UO_2$, which has been doped to produce a larger grain size than conventional $UO_2$. To enhance grain growth of $UO_2$ during sintering, fuel vendors have begun to add small amounts ( $\sim$ 0.1 wt%) of $Cr_2O_3$ or $Cr_2O_3$ and $Al_2O_3$ resulting in grain sizes of $\sim$ 40-70 $\mu m$ [1, 2]. It is advantageous to limit the dopant concentration to the solubility limit, to maintain the benefit of large grains without sacrificing the important properties of $UO_2$. The larger grain sizes provide improved operational fuel behavior for fission gas retention and pellet-cladding interactions due to improved mechanical properties [3]; one such property is creep.

Diffusional creep due to bulk (Nabarro-Herring) and grain boundary (GB) (Coble) are both reduced by an increase in grain size. Currently in BISON [4], the diffusional creep term, given by the empirical correlation MATPRO, only includes a Nabarro Herring grain size dependence [4]. However, due to the large migration barrier for uranium vacancies, low concentrations in the bulk and large segregation energies to the GB [5], it is highly likely that Coble creep must be accounted for. Therefore, by including Coble creep in a model that can be used in BISON, we can better describe creep behaviour in large grain doped $UO_2$.

Work has begun on addressing the parameters using atomistic data to inform Coble creep. For example, in a previous milestone [6], segregation energies and elastic dipole tensors components have been investigated for a uranium vacancy at various positions within different GBs. This is important because these describe the response of a defect energy to a stress, which governs the thermodynamic driving force for net diffusion of uranium vacancies along GBs due to an applied stress - a key component of Coble creep.

In this work, we use atomistic-scale data to develop an analytical creep rate model for $UO_2$, as a function of temperature and fission rate. From a previous report [7], Coble creep was suspected to be the dominant mechanism, therefore in this study, the focus of the atomistic simulations is to calculate contributions at the GB; such as uranium vacancy diffusivity and defect concentration. Due ot the grain size dependence of the creep model, by developing the model using various creep mechanisms, informed by processes at the atomic scale, the dominant creep mechanism can be identified and used in future work for predicting the creep rates in doped $UO_2$.

# 2 Theory and Methods

This section outlines the creep mechanisms that will be investigated in this work. Moreover, the simulation methods used, such as; structure creation, simulation parameters and diffusivity calculations, are also described.

## 2.1 Creep

In material science, creep is a type of plastic deformation that causes the permanent deformation of a solid material under stress. There are different mechanisms of creep and their influence depends on the material type, for example metals or ceramics. $UO_2$ is the material investigated in this report, where the possible creep mechanisms are diffusional creep and climb. Diffusional creep has two different contributions: i) bulk diffusion (Nabarro-Herring [8,9]) and ii) GB diffusion (Coble [10]). Both of these processes are driven by the net diffusion of uranium vacancies (although uranium interstitials may play an important role under irradiation conditions) arising from the chemical potential gradient induced by an applied stress. A schematic illustrating these two diffusional creep mechanisms is shown in figure 2.1.

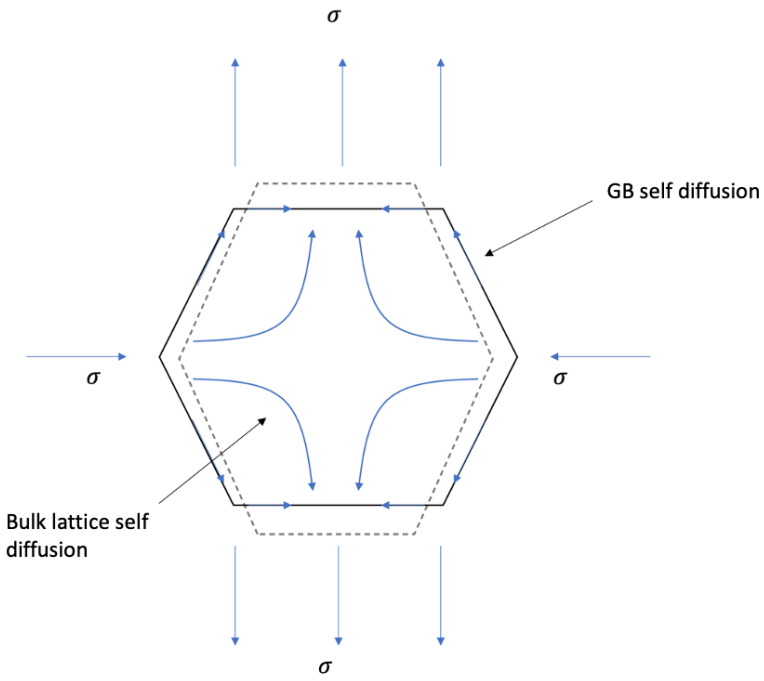


Figure 2.1: Schematic illustrating self-diffusional creep mechanisms occurring in a grain of $UO_2$.

### 2.1.1 Nabarro-Herring Creep

Nabarro-Herring (bulk diffusional) creep occurs via the bulk diffusion of point defects within a grain in response to an applied stress. Defect concentration gradients arise across the grain due to the influence of stress on a defect's chemical potential. For example, the energy of vacancies is typically lower in a compressive strain field and, therefore, will diffuse from tensile to compressive regions. Consequently, uranium atoms will self-diffuse in the opposite direction, resulting in the transport of mass to tensile regions. This process results in plastic deformation (creep) that acts to relive an applied stress. The Nabarro-Herring creep rate, due to a given defect $x$ can be approximated by the following equation:

$$\sigma_{NH,\,x} = \frac{42|\Omega_x|D_x[x]}{k_B T G^2}\sigma_v \tag{2.1}$$

where $\sigma_v$ is the von-Mises stress, $G$ is the grain size, $[x]$ is the defect concentration, $\Omega_x$ is the defect volume, $D_x$ is the diffusivity of defect $x$, $k_B$ is the Boltzmann constant and $T$ is temperature.

### 2.1.2 Coble Creep

Coble creep is similar to Nabarro-Herring creep, however, rather than occurring within the grain interior, it transpires at the GB. As with the Nabarro-Herring process, vacancies will diffuse (this time along the GB), from tensile to compressive regions leading to transport of mass and creep. The Coble creep rate due to a given defect, $x$, is given by:

$$\sigma_{Coble,\,x} = \frac{42|\Omega_{x,GB}|D_x^{GB}[x_{GB}]\pi\delta}{k_B T G^3}\sigma_v \tag{2.2}$$

where $[x_{GB}]$ is the defect concentration at the GB, $\Omega_{x,GB}$ is the defect volume at the GB, $D_x^{GB}$ is the is the diffusivity of defect at the GB $x_{GB}$ and $\delta$ is the GB thickness.

### 2.1.3 Climb-limited Dislocation Creep

The movement of dislocations at low stresses, which results in creep, is limited by the arrival or emission of defects that enable them to climb over an obstacle. This process occurs in the bulk similar to Nabarro-Herring creep. Climb-limited creep is described by:

$$\sigma_{Climb,\,x} = A_1 \frac{D_x[x]\mu b}{k_B T}\left(\frac{\sigma_v}{\mu}\right)^3 \tag{2.3}$$

where $A_1$ is a dimensionless constant (taken in this work to be exactly 1), $\mu$ (75 GPa) is the shear modulus, and $b$ is the Burgers vector (approximated by the lattice constant). $[x]$ and $D_x$ are the concentration and diffusivity, respectively, of defect $x$ in the bulk lattice.

## 2.2 Bulk Defect Concentration Calculations

A cluster dynamics model formulated in terms of the free energy of the system (free energy cluster dynamics or FECD) was developed by Matthews et al. [11] and is implemented in the Centipede code. Simulations using this cluster dynamics code have been applied here to calculate the diffusivity, $D_x$, and the concentration, [x], for a range of uranium defects (table 2.1) in bulk $UO_2$ under thermal equilibrium and irradiation conditions. The concentrations of defects in the $UO_2$ system under irradiation are calculated by solving a set of rate equations that describe process such as; clustering of point defects, creation and recombination of Frenkel pairs and interactions with sinks. A more detailed description of Centipede can be found in [11].

The defects that the Centipede code predicts the concentrations ([x]) and diffusivities ($D_x$) for are shown in table 2.1. Only uranium vacancy defects with a negative defect volume and, conversely, uranium interstitial defects with a positive defect volume are included, as these are the ones that cause creep. The partial pressure as a function of temperature was taken as the "best case" from Matthews et al. [11], at a value of $H_{PO2}$ =5.9 eV and $T_0$=2373 K. The "best case" conditions produced self-diffusivity data that matches the Sabioni et. al uranium self-diffusion experimental data [12]. The predicted concentrations were then probed as a function of fission rate in the range $10^{16}$-$10^{21}$ fissions/m$^3$s.

Table 2.1: Uranium defect types and their corresponding absolute values of the atomic volumes.

| $\text{Defect}_x$ | $\lvert\Omega_x\rvert$ (m$^3$) |
|---|---|
| $U_i$ | $5.99009\times10^{-29}$ |
| $U_i : 2O_i$ | $2.54003\times10^{-29}$ |
| $v_U$ | $8.6013\times10^{-30}$ |
| $v_U : v_O$ | $2.5991\times10^{-30}$ |
| $v_U : 2v_O$ | $9.3579\times10^{-30}$ |
| $2v_U : 2v_O$ | $4.8166\times10^{-29}$ |

## 2.3 GB Defect Concentration Calculations

To have an equation describing the concentration of defects at the GB, the segregation energy of defects to the GB needs to be known;

$$E_{Seg} = E_{f_{GB}} - E_{f_{Bulk}} \tag{2.4}$$

where $E_{Seg}$ refers to the segregation energy, $E_{f_{Bulk}}$ is the formation energy of the defect in the bulk and $E_{f_{GB}}$ is the formation energy of the defect at the GB.

Then the concentration of defects at the GB can be described by:

$$[x_{GB}] = exp\left[\frac{-(E_{f_{Bulk}} + E_{Seg})}{k_B T}\right] \tag{2.5}$$

alternatively, if the bulk concentration is know, it can be expressed as:

$$[x_{GB}] = exp\left[\frac{-E_{Seg}}{k_B T}\right][x] \tag{2.6}$$

where $[x_{GB}]$ is the concentration of defects at the GB and $[x]$ is the concentration of defects in the bulk.

## 2.4 MD Procedure

In this report, molecular dynamics (MD) simulations are carried out using the large-scale atomic/molecular massively parallel simulator (LAMMPS) [13], where the interatomic forces between all the uranium and oxygen atoms were described using the Cooper, Rushton and Grimes (CRG) potential [14]. This combines a pair potential with a many body contribution using the embedded atom method of Daw and Baskes [15].

### 2.4.1 GB Structure Creation

A GB is a surface defect that separates two crystalline grains with different orientations. For this work, symmetrical tilt grain boundaries were generated with a rotation angle θ equal to half the misorientation angle. Two tilt grain boundaries were considered for this study and are outlined in table 2.2. Due to the periodic boundary conditions, each simulation box contains two grain boundaries in the (y, z) plane, separated by a distance equal to half the box size along the x-direction. A Σ9 tilt GB structure is shown in figures 2.2a (coloured by atom species) and 2.2b (coloured by coordination number - allowing the GB thickness to be clearly visualized). To study the effect of uranium vacancy diffusion at a GB, structure creation following a similar procedure as outlined in a previous NEAMS milestone [6] was undertaken. First, the lowest energy structure for each GB without any defects was found by sampling the γ-surface and energy minimizing the system (described later in section 2.4.2). Then, a concentration of uranium vacancies (or interstitials) were randomly added to the GB within 1 nm thick slabs and the structure energy minimized.

Table 2.2: Supercell dimensions for GB structures. $GB_1$ outlines the structures used for the diffusivity calculations in section 3.1.1. Whereas, $GB_2$ is the GB structure used for the longer diffusivity calculations in section 3.1.2 - where the bulk (x-direction) has been reduced. Each value refers to the x, y and z direction (i.e. $L_x \times L_y \times L_z$) with the units in $\AA$.

| Grain boundary | $GB_1$ | $GB_2$ |
|---|---|---|
| Σ9-(221) | 186.3×131.0×38.5 | 140.0×131.0×38.5 |
| Σ5-(210) | 172.9×138.0×109.1 | - |

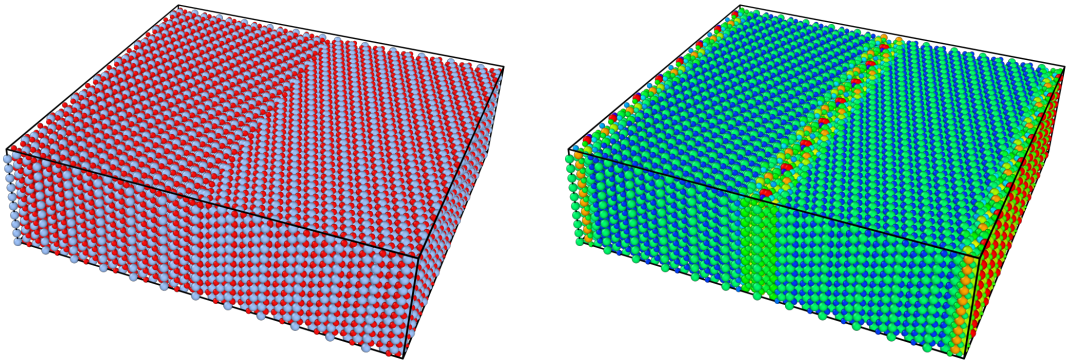

(a) (b)

Figure 2.2: (a) A Σ9 tilt grain boundary structure, where the red speheres represent the oxygen atoms and the blue spheres represent the uranium atoms. (b) A Σ9 tilt grain boundary structure where the spheres represent atoms coloured by coordination number.

### 2.4.2 GB Minimization

To determine the lowest energy structure of a GB structure without defects, all atoms for one grain were shifted in the y-z plane with 0.5 Å increments in the y and z directions. For each increment, the system was energy minimized at zero pressure allowing the GB gamma surface to be sampled. Following this, the lowest energy structure was chosen and defects (uranium vacancies or uranium interstitials) were randomly added to the GB at a specific concentration. In the case of uranium vacancies, to observe the effects of different charge compensation mechanisms, structures containing $V_O^{\bullet\bullet}$ (Kröger-Vink notation [16]) by removing oxygen atoms, $U_U^{\bullet}$ (electron holes) by converting some $U^{4+}$ cations to $U^{5+}$ describing the oxidation of $U^{4+}$, and applying a background charge were all created.

### 2.4.3 Diffusivity Calculations

The temperature dependence of the self-diffusion coefficient frequently can be described by an Arrhenius relationship for a single diffusion mechanism, when $H_a$ and $D_{0,self}$ are constant.

$$D_{self} = D_{0,self}\ exp\left(\frac{-H_a}{k_B T}\right) \tag{2.7}$$

$D_{0,self}$ is the pre-exponential and $H_a$ is the activation enthalpy. For self-diffusivity, the activation enthalpy is the sum of the formation and the migration enthalpies. The formation energy is the energetic cost to create a defect in a lattice (that facilitates the diffusion process) and the migration energy is the energy barrier between an initial state and a final state of the diffusion process (for a system with a complex potential energy landscape, there may be a number of different paths that need to be considered).

The mean squared displacement of atoms during MD simulations is used to calculate the diffusivity values of uranium atoms (which, given the vacancy concentration, can be used to obtain

uranium vacancy diffusivity). Generally, the mean-square displacement becomes a linear function of time as time increases so that the diffusion constant is simply related to the slope of this linear regime. It is important to run the simulation long enough that the linear regime is reached, a point that will be discussed later.

The uranium defect diffusivity, $D_x^{GB}$ is determined at the GB using the following equation:

$$D_x^{GB} = \frac{N_{supercell}}{N_{GB}} \left( \frac{\langle R_{U_{yz}} \rangle}{4t} \right) \left( \frac{1}{[x_{GB}]} \right) \tag{2.8}$$

where $N_{supercell}$ is the total number of atoms in the system, $N_{GB}$ is the number of atoms in the GB, $\langle R_{U_{yz}} \rangle$ is the mean squared displacement for uranium atoms in the yz plane, $t$ is time and $[x_{GB}]$ is concentration of defects, $x$, at the GB (percentage of uranium defects with respect to uranium sites in the GB).

Following GB energy minimization and addition of defects, an MD run with an isobaric-isothermal (NPT) ensemble was carried out for 80 ps. The first 40 ps was used to bring the system up to the desired temperature and then the system was allowed to equilibrate at the target temperature for 40 ps. An average of the lattice parameter was taken over the last 6 ps and the systems lattice parameter was changed to the obtained average. The simulation was then run for a canonical (NVT) ensemble for 20 ps at the desired temperature and a microcanonical ensemble (NVE) for 10 ns for results shown in section 3.1.1 and 70 ns for results shown in section 3.1.2. From this, the mean squared displacement for uranium was calculated and the uranium vacancy diffusivity was determined using equation 2.8.

# 3 Results and Discussion

An atomistic informed creep model for $UO_2$ was developed in a previous milestone [7]. It was found that Nabarro-Herring and climb creep rates were far too low to describe $UO_2$ creep rates predicted by the empirical MATPRO correlations [4], which are applied in BISON. Although Coble creep rates were also orders of magnitude too low to capture expected creep rates in $UO_2$, there were a number of uncertainties in modeling the Coble creep rate, that when resolved, may improve the comparison with experiment. In particular, the elastic dipole tensor of GB defects, as well as the enhanced concentration and mobility of GB defects could all result in higher creep rates.

In this section we aim to improve upon the previous creep model by using atomistic simulations to calculate $D_{V_U}^{GB}$ (and $D_{U_i}^{GB}$), predicting the defect concentrations at the GB (under thermal equilibrium and irradiation conditions) and applying the new atomistic data to different creep mechanisms comparing the results to both MATPRO correlations and experiment.

## 3.1 Diffusivity

The prediction of $D_{V_U}^{GB}$ and $D_{U_i}^{GB}$ are outlined below. This section is broken up into two parts ('Simulating $\mathrm{D}_{\mathrm{V_U}}^{\mathrm{GB}}$ at Two Tilt GBs' and 'Improved Long-Range Diffusivity'). Bulk diffusivity values were calculated for each contributing defect type using the cluster dynamics code Centipede [11], as described in section 2.2.

### 3.1.1 Simulating $\mathrm{D}_{\mathrm{V_U}}^{\mathrm{GB}}$ at two Tilt GBs

The uranium vacancy diffusion coefficient was calculated at two grain boundaries (Σ5 tilt and Σ9 tilt), using three different charge compensation mechanisms ($\mathrm{V}_{\mathrm{O}}^{\bullet\bullet}$, $\mathrm{U}_{\mathrm{U}}^{\bullet}$ and applying a net background charge) by the method outlined in section 2.4.3. Furthermore, different concentrations and temperatures were examined to see if they impact the predicted uranium vacancy diffusivity, making sure to capture the correct uranium vacancy diffusion values at the point defect limit. A concentration of 0.25% uranium defects was decided to be used to ensure there were no interactions between the defects. Using MD, there needs to be enough defects in the system, at a temperature where defects can hop frequently, so that sufficient statistics can be obtained to calculate a $D_{V_U}^{GB}$ value during timescales associated with MD (on the order of ns).

By plotting $D_{V_U}$ on a log scale as a function of 1/T, as presented in figure 3.1, the diffusion at the GB can be compared to that in the bulk (predicted from DFT [11]). Figure 3.1 shows that, for each GB case, $D_{V_U}$ is orders of magnitude greater than that in the bulk. This result indicates

that Coble creep rates will be shifted to higher values compared to the Nabarro-Herring creep rates and may help with the previous issue, where atomistic informed creep rates were orders of magnitude lower than the MATPRO correlations - a point that will be discussed in greater detail later in this report.

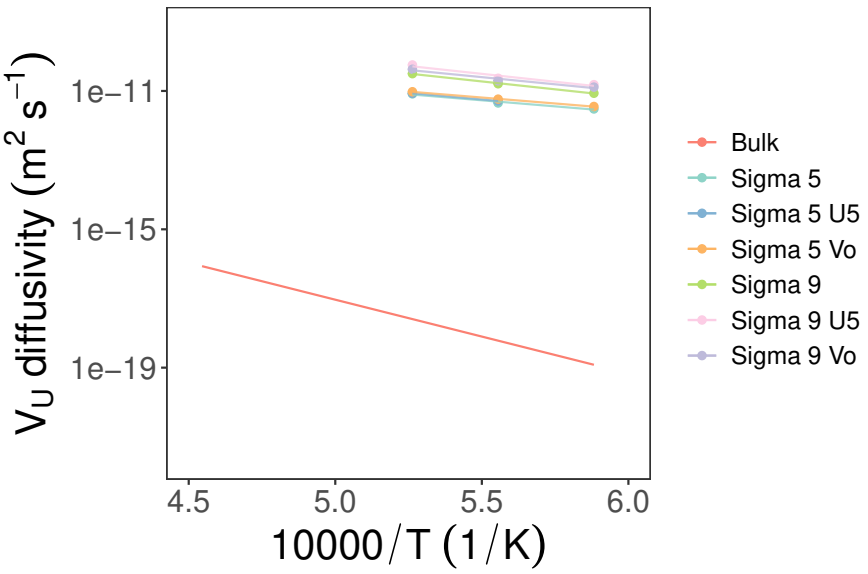


Figure 3.1: Arrhenius plot of uranium vacancy diffusion coefficient as a function of inverse temperature. The red line represents the diffusion coefficient in the bulk (calculated from DFT [11]), while the other coloured points are diffusion coefficients for grain boundaries with different charge compensation mechanisms.

$D_{V_U}^{GB}$ shown in figure 3.1 are presented in figure 3.2, separated by GB type. From this, it is observed that different GBs will have different $D_{V_U}^{GB}$ values (still orders of magnitude greater than the bulk), however, the choice of charge mechanism used does not greatly impact the diffusivity.

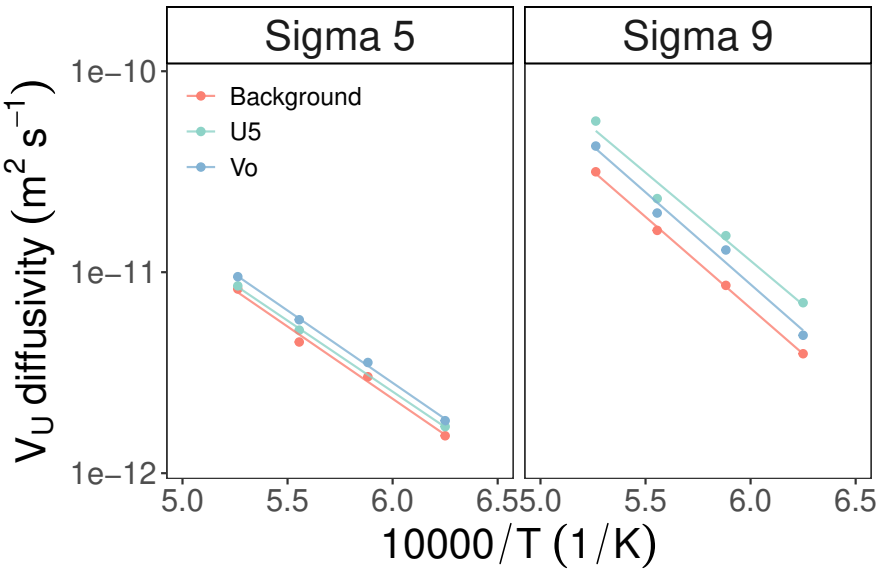


Figure 3.2: Arrhenius plot of uranium vacancy diffusion coefficient as a unction of inverse temperature for two GB structures from figure 3.1. The blue points are values for an oxygen charge compensation mechanism, the green points are values for a $U^{5+}$ compensation mechanism and the red points represent a net background charge.

### 3.1.2 Improved Long-Range Diffusivity

Analyzing the uranium vacancy trajectories using Ovito [17], it was found that the simulations did not capture the long range diffusion of uranium vacancies. A gradient for the MSD runs was observed at $\sim$10 ns (see figure 3.3) because some of the uranium atoms at the GB found low energy paths (due to the nature of the GB structure). However, this happens at localized pockets and does not describe the true long range diffusion of uranium.

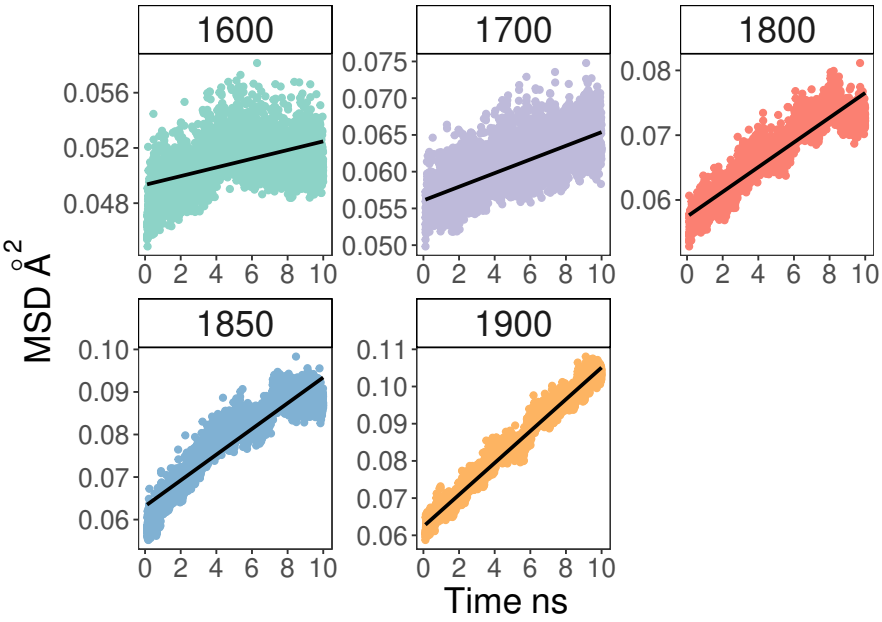


Figure 3.3: Mean squared displacement of uranium atoms in a Σ9 tilt GB containing uranium vacancies at different temperatures for a 10 ns simulation run.

To improve the statistics and capture long range diffusion of the uranium vacancies we chose one GB (Σ9), ran the simulations for a longer time (∼70 ns), decreased the structure size (by removing some of the bulk) and took advantage of the two GBs in our system (the GB at the system center and at the periodic boundary) by introducing uranium vacancies in both to improve statistics. As the type of charge compensation mechanism did not greatly affect $D_{V_U}^{GB}$, shown in section 3.1.1, the charge compensation mechanism applied was a net background charge and the concentration of uranium defects was 0.25% of uranium sites at the GB.

Figure 3.4a shows the MSD for uranium atoms at the Σ9 tilt GB structure (the uranium atoms do not move in the bulk because there are no vacancies there) across the temperature range 1600-1900 K. It can be seen that for lower temperatures (<1800 K) a timescale of ∼70 ns was needed to achieve enough statistics to observe proper linear behaviour, and therefore, capture long range diffusion at the GB. The MSD was then used in equation 2.8 to calculate $D_{V_U}^{GB}$, shown as a function of temperature in figure 3.4b. This results in a better description of Arrhenius behaviour with less scatter of the data-points allowing for a more accurate migration energy and $D_0$ to be calculated, presented in table 3.1. This has an important impact on the creep rates and will be discussed in section 3.3.1.

The same procedure outlined above for uranium vacancies was also conducted for uranium interstitials. The MSD of the uranium atoms are shown in figure 3.5a, with the corresponding uranium interstitial diffusion coefficient presented in figure 3.5b. Although the data-points are more scattered for the uranium interstitials compared to the vacancy case, a sufficient diffusion

fit can be calculated (table 3.1) - this should be improved in future simulations.

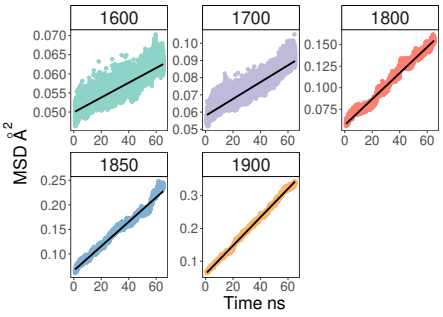


(a)

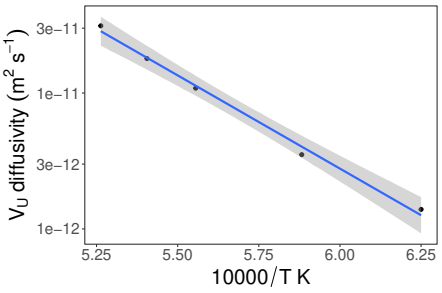


(b)

Figure 3.4: (a) Mean squared displacement of uranium atoms in a Σ9 tilt GB containing uranium vacancies at different temperatures. (b) Uranium vacancy diffusion coefficient as a function of inverse temperature in a Σ9 tilt GB. The grey band represents the 95% confidence level interval for $D_{V_U}$ predictions from the linear fit (blue line).

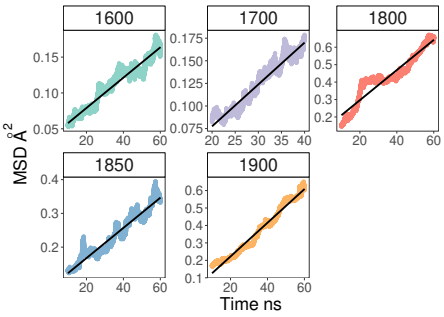


(a)

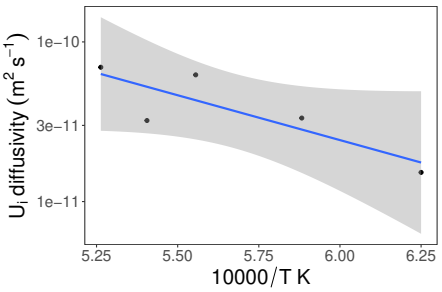


(b)

Figure 3.5: (a) Mean squared displacement of uranium atoms in a Σ9 tilt GB containing uranium interstitials at different temperatures. (b) Uranium interstitial diffusion coefficient as a function of inverse temperature in a Σ9 tilt GB. The grey band represents the 95% confidence level interval for $D_{U_i}$ predictions from the linear fit (blue line).

Table 3.1: Pre-exponential and migration energy values calculated from figures 3.4b and 3.5b.

| Defect | $D_0^{GB}$ $m^2/s$ | $E_{mig}$ eV |
|---|---|---|
| $D_{V_U}^{GB}$ | $4.74\times10^{-4}$ | 2.72 |
| $D_{U_i}^{GB}$ | $5.70\times10^{-8}$ | 1.12 |

## 3.2 Segregation Energy Model

In a previous milestone, Andersson et al. [5] used atomistic simulations to calculate segregation energies as a function of GB concentration for uranium vacancies at different types of

grain boundaries (Σ5 tilt, Σ5 twist and a high angle random boundary) in $UO_2$ (shown in figures 3.6a, 3.6b and 3.6c). This same method was also used to calculate the segregation energies as a function of GB concentration of Xe atoms at GBs [5, 18].

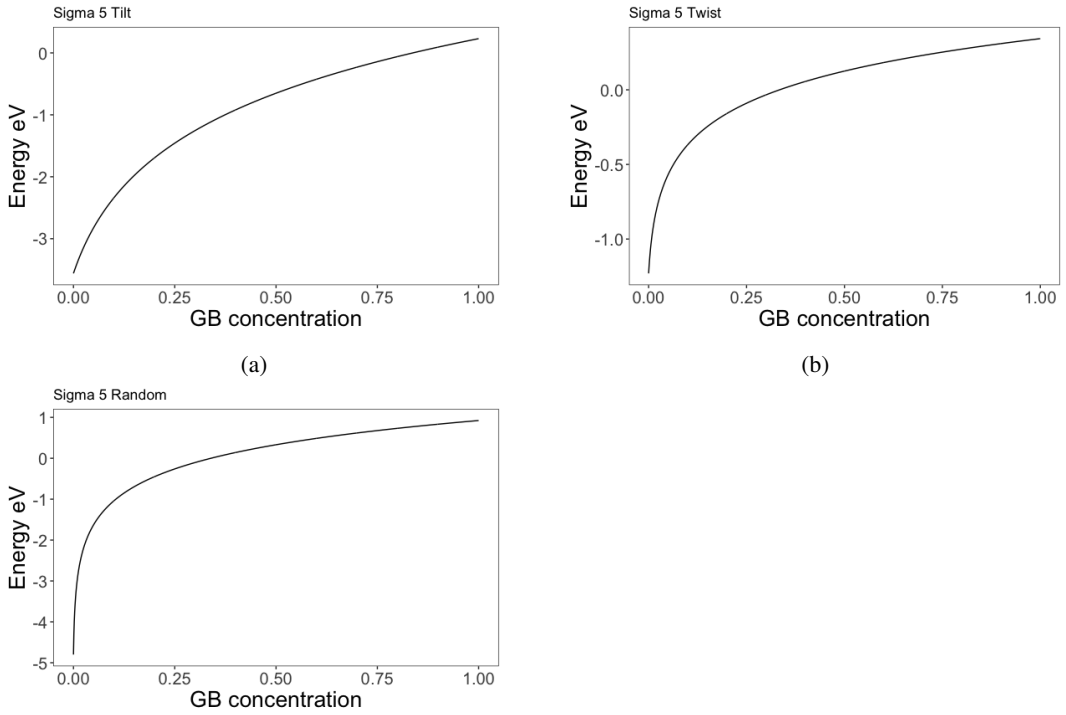


Figure 3.6: (a) The concentration dependence of the $V_U''''$ segregation energy at a Σ5 tilt GB. (b) The concentration dependence of the $V_U''''$ segregation energy at a Σ5 twist GB. (c) The concentration dependence of the $V_U''''$ segregation energy at a high angle random GB structure.

As mentioned earlier in this report, a previous atomistic informed creep model assumed that an enhancement factor of six orders of magnitude was applied to the GB self-diffusivity compared to the bulk, without resolving whether it was acting on the concentration of defects, the diffusion of defects, or both. Here, using the segregation energy models developed by Andersson et al. [5], the concentration of defects at the GB can be predicted. A schematic outlining this process is illustrated in figure 3.7. This procedure is set out in 3 stages: i) using one of the segregation energy models (shown in figures 3.6a, 3.6b and 3.6c), a segregation energy related to a specific GB concentration is chosen. ii) For a specific bulk defect concentration at temperate $T$, this segregation energy is used to calculate the equilibrium defect concentration at the GB (equation 2.6). iii) If the GB concentration from equation 2.6 matches that used in the segregation energy model, then the self-consistent solution has been found. Otherwise a new segregation energy is chosen and process is repeated. Stages i) and ii) can be repeated using updated segregation energies until a satisfactory match is achieved.

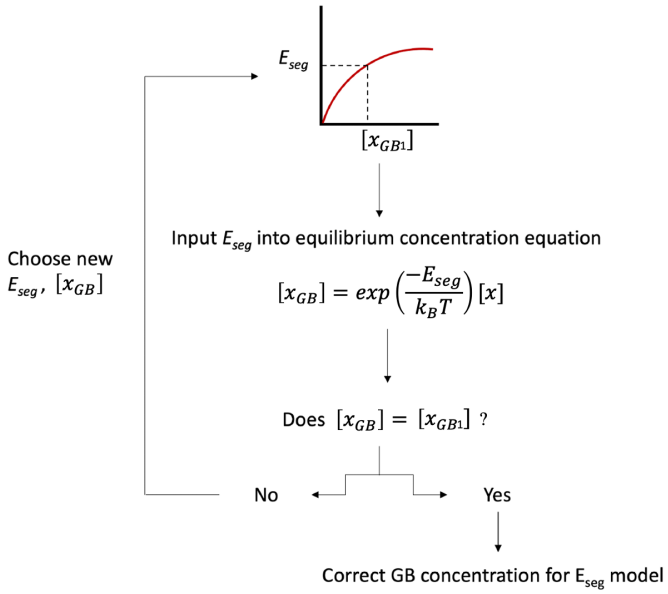


Figure 3.7: A schematic illustration of the procedure to calculate the defect concentration at the grain boundary, using the bulk defect concentration and concentration dependent segregation energies as inputs.

The concentration of defects in the bulk $[Bulk_x]$ used in equation 2.6 were calculated from Centipede cluster dynamics simulations as described in section 2.2.

## 3.3 Analytical Creep Model

In this section, the lower length-scale atomistic data is put into the analytical creep equations 2.1, 2.2 and 2.3, and the creep rates of $UO_2$ for the various mechanisms as a function of temperature, at a specific grain sizes and stress are examined. It is important to distinguish among the various creep mechanisms, given that they have different grain-size dependencies.

### 3.3.1 Impact of GB Diffusivity on Coble Creep Rate

Figure 3.8 shows the creep rates in $UO_2$ for different creep mechanisms as a function of inverse temperature, for a grain size of 27 $\mu$m and a stress of 30 $\times 10^6$ Pa. The creep rate for the existing MATPRO model in BISON (solid green line for thermal equilibrium and solid orange line for irradiation) is also included. Similar to the previous creep model [7], Nabarro-Herring and climb creep are orders of magnitude below the empirical MATPRO correlation. However, when $D_{V_U}^{GB}$ calculated from MD is input into Coble creep (equation 2.2), then enhanced creep rates (solid and dashed purple lines) are observed. In fact, these enhanced Coble creep rates over-predict compared to the MATPRO correlation (solid green line). The solid purple line uses the diffusion value from section 3.1.1 while the dashed purple line uses the diffusivity value from the longer

simulation run described in section 3.1.2. Other parameters used in equation 2.2 to produce figure 3.8 were the defect concentration, estimated to be six orders of magnitude greater at the GB compared to in the bulk, and the atomic volumes of the defects (uranium vacancy defects-table 2.1).

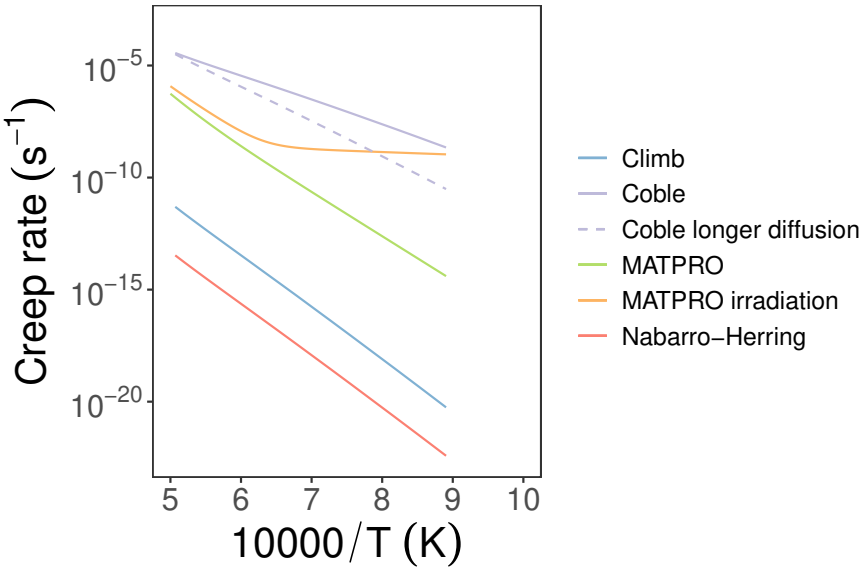


Figure 3.8: Arrhenius plot of creep rate as a function of inverse temperature for $UO_2$ comparing the atomistic informed creep mechanisms with the empirical MATPRO correlation for a grain size of 27 $\mu$m and a stress of 30 $\times 10^6$ Pa.

### 3.3.2 Impact of Defect Concentration at the GB on Coble Creep Rate

Presented in figure 3.9 are the $UO_2$ creep rates for various creep mechanisms (similar to figure 3.8); however, the GB defect concentrations (section 3.2) are included in the Coble creep analytical equation (using the diffusivity value calculated in section 3.1.2). Furthermore, uranium interstitial defects, their corresponding atomic volumes and the predicted uranium interstitial diffusion coefficient (calculated in section 3.1.2) were also incorporated. The concentration of interstitial defects at the GB were calculated using the uranium vacancy segregation energy models (section 3.2), an assumption which is deemed acceptable in the absence of an interstitial specific model to achieve preliminary results for this creep model, but needs to be improved for future work. There are three Coble creep models referring to the different defect concentrations at the GB calculated from the three segregation energy models (figures 3.6a, 3.6b and 3.6c). The inclusion of the calculated GB defect concentration along with the diffusivity values calculated at the GB gives a much improved comparison with the MATPRO correlation for stoichiometric $UO_2$. From the three Coble creep models, 'model 3' gives the best comparison. Model 3 also predicts sensible defect concentrations $\sim$1% at the GB compared to model 1 and 2 which predict concentrations of $\sim$30%. Although the creep rate gradient of Coble model 3 (pink dashed line) is different from the MATPRO correlation (solid green line), the defect concentrations used in

the creep analytical equations calculated here are for a oxygen partial pressure, deviating very slightly from stoichiometry (the "best case" values used in Matthews et. al [11]), while the MATPRO correlation is assumed to be at exactly stoichiometric $UO_2$. As mentioned earlier, "best case" refers to the oxygen partial pressure which best matches the Sabioni et al. [12] uranium self-diffusion data.

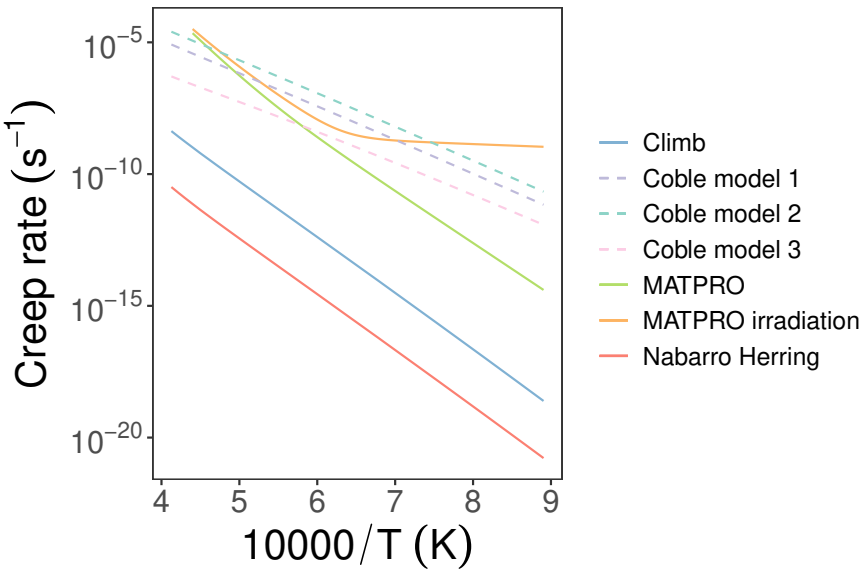


Figure 3.9: Arrhenius plot of thermal equilibrium creep rate as a function of inverse temperature for $UO_2$. The dashed lines represent the three different Coble creep models for the concentration dependent segregation energy models of three GBs.

Figure 3.10 compares Coble creep model 3 with the MATPRO correlation and with experiment [19] for four different cases (outlined in table 3.2). Overall, there is a good agreement for each case, whereby further improvements can be made in the analytical equations by adjusting the partial pressure conditions when calculating the bulk defect concentrations from Centipede (which are put into the concentration dependent segregation energy model to predict defect concentrations at the GB).

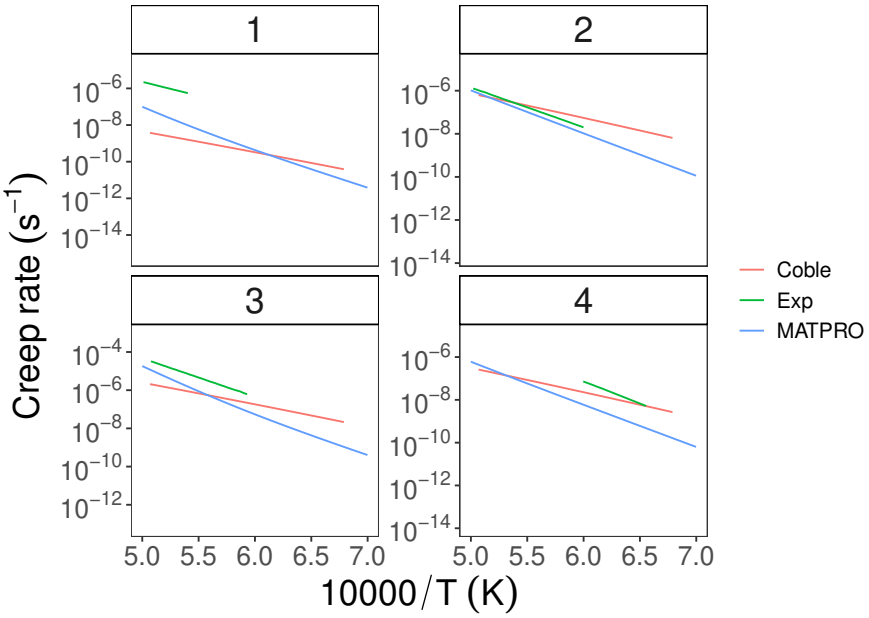


Figure 3.10: Arrhenius plot of creep rate as a function of inverse temperature for $UO_2$, comparing the atomistic developed Cobel model 3 with MATPRO and experiment for four different cases outlined in table 3.2.

Table 3.2: Different experimental case study parameters [19] used for comparison in figure 3.10.

| Case | Grain size ($\mu$ m) | Stress (MPa) |
|---|---|---|
| 1 | 55.0 | 20.7 |
| 2 | 10.0 | 20.7 |
| 3 | 10.0 | 68.9 |
| 4 | 13.4 | 20.7 |

Chung and Davies [20] report low-stress diffusional creep response for $UO_2$ at temperatures ranging from 1273 - 1873 K for different grain sizes (2–10 µm). Using this data, figure 3.11 compares creep rates with the atomistic informed Coble creep model developed in this study, as a function of stress for a 2 $\mu$m grain.

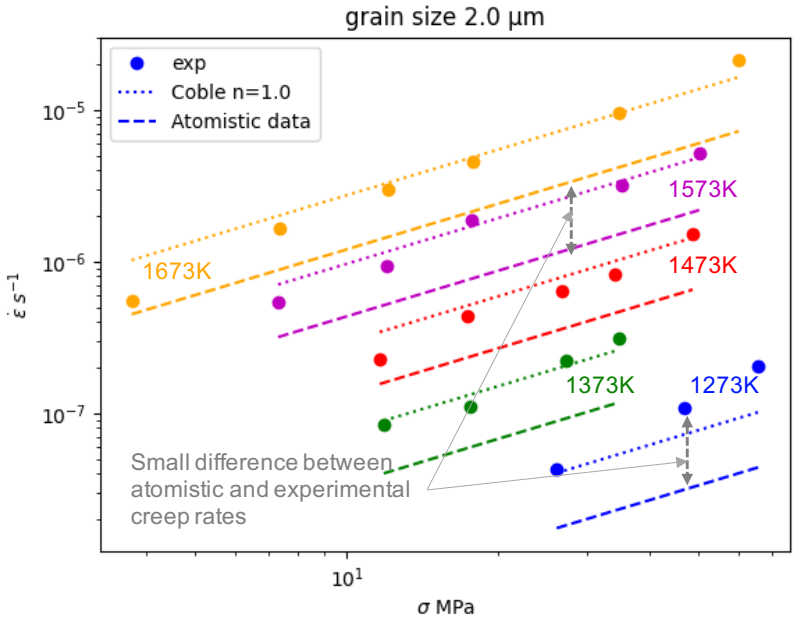


Figure 3.11: Comparison of steady state creep rates using the diffusion parameters fit to experimental data-points and assuming pure Coble creep (*Coble* $n = 1.0$, dotted lines), with the creep rates obtained using diffusion parameters from atomistic simulations (dashed lines) at different temperatures. The markers are the corresponding experimental data reported in [20]. There appears to be negligible difference ($\approx 2.0$) between the creep rates from experimental and atomistic diffusion data for the grain boundary dominated creep regime (grain size: 2 µm).

### 3.3.3 Irradiation Conditions

In this section, creep rates of $UO_2$ under different irradiation conditions are calculated and compared with the MATPRO irradiation case, shown in figures 3.12 and 3.13. To calculate creep rates under irradiation conditions, bulk concentrations were re-calculated using the cluster dynamics code Centipede under the same partial pressure conditions as before for different fission rates. These bulk concentrations under irradiation conditions were then implemented in the segregation energy model (using model 3) as outlined in section 3.2 to calculate the defect concentrations at the GB under irradiation. A fit given by equation 3.1 was formulated to capture the total creep rates (produced by a Coble mechanism which is the dominant creep mechanism) as a function of temperature and fission rate density, as displayed in figure 3.12 (for a grain size of $27\times10^{-6}$ m, GB thickness of $1\times10^{-9}$ m, and stress of $30\times10^{6}$ Pa).

$$\sigma_{Coble,\,x} = \frac{42\pi\delta}{k_B T G^3}\sigma_v \left[ A_1 exp\left(\frac{-B_1}{k_B T}\right) + A_2 exp\left(\frac{-B_2}{k_B T}\right)\dot{F}^{0.3} + A_3\dot{F}^{0.6} \right] \tag{3.1}$$

where $A_1$, $A_2$, $B_1$, $B_2$ and $A_3$ are fitting parameters, $\dot{F}$ describes the fission rate (in fissions/$m^3$s), $\sigma_v$ is the von-Mises stress in Pa, $G$ is the grain size in m, $\delta$ is the grain boundary thickness in m, $k_B$ is the Boltzmann constant in J/K and $T$ is temperature in K.

The parameters used in equation 3.1 are displayed in table 3.3.

Table 3.3: Fitting parameters used in equation 3.1.

| $A_1$ ($m^5/s$) | $A_2$ $(m^3/s)^{0.3}$ | $A_3$ $(m^3/s)^{0.6}$ | $B_1$ (J) | $B_2$ (J) |
|---|---|---|---|---|
| $1.20\times10^{-35}$ | $4\times10^{-45}$ | $2.5\times10^{-56}$ | $3.94\times10^{-19}$ | $2.00\times10^{-19}$ |

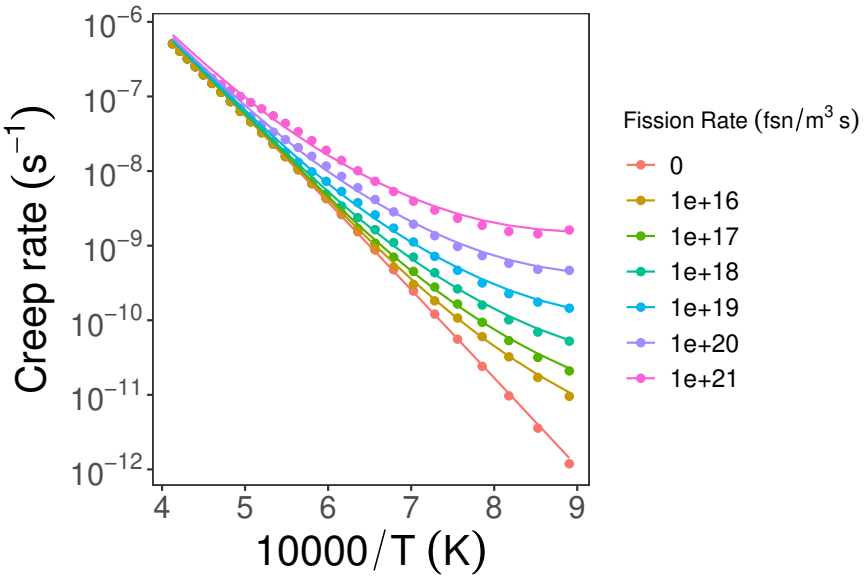


Figure 3.12: Predicted atomistic informed creep rates as a function of inverse temperature and fission rate density. The solid lines represent the fit described in equation 3.1.

For clarity, figure 3.13 shows the thermal equilibrium, and irradiation case for typical LWR fission rates ($10^{19}$fissions/$m^3$/s). There is an excellent improvement of the Coble creep rate in relation to the MATPRO correlation under irradiation. As mentioned previously, one discrepancy between the MATPRO correlation and the atomistic informed creep model is the stoichiometry. For MATPRO, the $x$ in $UO_{2+x}$ is assumed to be zero, whereas using Centipede $x$ varies as a function of temperature. The Centipede partial pressure conditions were optimized to produce self-diffusivity data that matches the Sabioni et. al uranium self-diffusion experimental data [12]. However, by adjusting the partial pressure values a better match to MATPRO (and experimental) creep rates can be achieved. Furthermore, as mentioned, the concentration of interstitial defects at the GB were calculated using the uranium vacancy segregation energy models (section 3.2), an assumption which is valid to get an preliminary result for this model, but will be improved in future simulations.

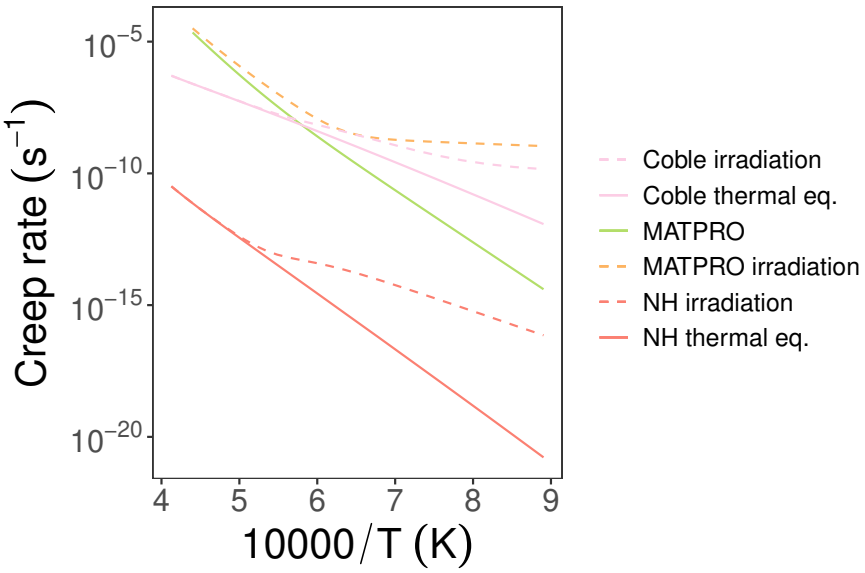


Figure 3.13: Arrhenius plot of creep rates at thermal equilibrium (solid lines) and under irradiation (dashed lines) as a function of inverse temperature for $UO_2$.

## 3.4 Full–field Simulations of Diffusion Creep in Uranium Dioxide

Diffusion mediated creep deformation in $UO_2$ is a particularly challenging problem depending on local defect concentrations, as well as the microstructure of the material (grain size, stoichiometry, and oxygen partial pressure). Therefore, there is a need to develop advanced microstructural sensitive material models that account for such local effects, and also consider the kinetics *and* kinematics of the diffusion mediated processes. In this section, a chemo-mechanically coupled point-defect diffusion model in a crystal plasticity framework to predict the structural response of $UO_2$ that considers the effect of the microstructure and the local defect concentration both in the grain bulk and in the boundary is proposed. Atomic-scale simulations used to understanding fundamental mechanisms governing physical properties, such as those calculated above (e.g. diffusion coefficients) and in previous milestones [6] (e.g. elastic dipole tensor) are used to inform this model. As a first step, preliminary full-field creep simulations with two-dimensional polycrystalline $UO_2$ are perfromed, with the dominant deformation mechanism reported.

The simulations outlined below simulates creep in polycrystalline uranium dioxide using a chemo-mechanically coupled defect diffusion model in a elasto-viscoplastic fast Fourier transform (EVPFFT) framework. The formulated model accounts for the kinematic response due to the diffusion process by tracking the local concentration of the defect species both in the grain boundaries *and* in the grain bulk. The EVPFFT framework also allows to incorporate plasticity due to dislocation climb, and climb assisted dislocation glide on the overall mechanical response of the material. Moreover, as mentioned above, the model is multi-scale in nature, and hence,

includes information from the lower scale atomistic simulations such as the local defect interaction (elastic dipole) tensor, that determines the local interaction energy due to diffusion of vacancies/atoms during the creep process [21]. Following briefly highlights the important field equations of the chemo-mechanically coupled model.

### 3.4.1 Kinematic and Constitutive Equations of the Multi-physics EVPFFT Framework

The continuum-level crystal plasticity framework is based on small-strain kinematics, where the total strain rate, $\dot{\varepsilon}$, is additively decomposed into elastic, $\dot{\varepsilon}^{el}$, and plastic, $\dot{\varepsilon}^{p}$, strain rates,

$$\dot{\varepsilon} = \dot{\varepsilon}^{el}_{ij} + \dot{\varepsilon}^{p}_{ij} \tag{3.2}$$

The total strain tensor, $\varepsilon$, is the symmetric part of the displacement gradient, $u_{i,j}$,

$$\varepsilon_{ij} = \varepsilon_{ji} = \frac{1}{2}\left(u_{i,j} + u_{j,i}\right) \tag{3.3}$$

The total plastic strain rate is given by the additive contributions from vacancy diffusion, dislocation climb, and dislocation glide,

$$\dot{\varepsilon}^{p}_{ij} = \dot{\varepsilon}^{dif}_{ij} + \dot{\varepsilon}^{cl}_{ij} + \dot{\varepsilon}^{dis}_{ij} \tag{3.4}$$

For the present model, diffusion-mediated strain rate, $\dot{\varepsilon}^{dif}$, is through diffusion of uranium vacancies and is facilitated by the local change in the vacancy concentration, as well as by the gradient in the local vacancy flux under a gradient in chemical potential. These respectively contribute to the dilatational and deviatoric components of the diffusion strain rate, $\dot{\varepsilon}^{dif}$ as [22, 23]:

$$\dot{\varepsilon}^{dif} = -\Omega_0 \left( \frac{\nabla j + \nabla j^T}{2} - \frac{\dot{c}\delta_{ij}}{3} \right) + \lambda_0 \Omega_0 \dot{c} \delta_{ij} \tag{3.5}$$

In this equation, $\nabla$ and $\delta_{ij}$ are the gradient and the Kronecker delta operators, while $\dot{c}$ and $j$ correspond to the local change in vacancy concentration and its flux, respectively. The flux, $j$, is gradient of chemical potential whose form is derived from continuum thermodynamics principles, and is excluded in the report for brevity. Moreover, in the current formulation, the transport equation for concentration evolution, $\dot{c}$, has additional terms relating to vacancy absorption by dislocations (climb), and the exchange between GB and bulk, along with the chemical potential (also not discussed here for brevity). $\Omega_0$ is the atomic volume and $\lambda_0$ corresponds to the isotropic stress equivalent of the elastic dipole tensor, $P$ which is related to the point-defect relaxation volume through the elastic compliance tensor, and provides the interaction energy of the point-defect with an external strain field as shown in [21]. The value of $P$ or $\lambda_0$ is obtained from the atomistic simulations performed in this work, and is different in the GB and in the bulk. Moreover, as also shown previously, different grain boundaries can have different values of this dipole tensor, which can be significantly different. For simplicity, we assume same value of this dipole tensor, $\lambda_0$, for all the boundaries in the continuum scale.

Plastic relaxation via dislocation climb occurs only in the bulk, and is considered only from edge dislocations. The strain rate due to dislocation climb thus depends on the local edge dislocation density in dislocation cells, $\rho^s_{cell,edge}$, and the climb velocity, $v^s_{climb}$, for the different slip systems, $s = 1, S$, where $S$ is the total number of active slip systems:

$$\dot{\varepsilon}^{cl}_{ij} = \sum_{s=1}^{S} l^s_{ij} \bar{\dot{\beta}}^s \tag{3.6}$$

$$\bar{\dot{\beta}}^s = \rho^s_{cell,edge} b^s v^s_{climb} \tag{3.7}$$

$b^s$ is the magnitude of the Burgers vector and $l^s_{ij}$ corresponding to the climb tensor $(= b^s \otimes b^s)$ [24]. The $v^s_{climb}$ parameter depends on the net flux of vacancies due to the imbalance between the vacancy concentration near the dislocation core and the bulk of the material:

$$v^s_{climb} = \frac{\Omega_0}{b^s} D^{bulk} Z^s_v \left( c^{core}_v - c^{bulk} \right) \tag{3.8}$$

with $D^{bulk}$ and $Z^s_v$ representing bulk vacancy diffusivity and vacancy capture efficiency of the dislocation [25, 26]. $c^{core}_v, c^{bulk}$ are the equilibrium vacancy concentration at the dislocation core and the local bulk vacancy concentration, respectively. Thus, the kinetics of the diffusion process has an impact on the plasticity mediated by dislocation climb.

The dislocation glide model follows directly from [24], and is briefly mentioned for completion. The shear deformation from dislocation glide is due to the combined shear rate from dislocation slip in the different slip systems, under the imposed resolved shear stress, $\tau^s$:

$$\dot{\varepsilon}^{dis} = \sum_s m^s_{ij} \dot{\gamma}^s \tag{3.9}$$

$$\dot{\gamma}^s = \rho^s_{cell} b^s v^s \text{sign}\left(\tau^s\right) \tag{3.10}$$

where, $\rho^s_{cell}$, $v^s$ are the cell dislocation density and mean dislocation velocity for the different slip systems. $m^s_{ij}$ is the symmetric part of the Schmid tensor for the different slip systems, and, $\text{sign}\left(\tau^s\right)$ ensures thermodynamic consistency of the constitutive law by enforcing the direction of shear rate to be the same as the direction of glide [24].

Subsequently, uniaxial creep simulations of polycrystalline uranium dioxide are performed with the multi-physics framework.

### 3.4.2 Creep Behavior of Polycrystalline Uranium Dioxide

In this work, two-dimensional creep simulations of polycrystalline material, Fig. 3.14, are performed at a uniaxial creep stress of 20 MPa (similar to what is used by Chung and Davies [20]) and 1673K with the corresponding model parameters listed in Table 3.4. Figure 3.15 plots the results of the creep simulation for a geometry with average grain size of $\approx 100\,\mu$m under the imposed boundary conditions. From the strain rate plots, Fig. 3.15 (b), there appears to be an initial increase, followed by the expected decrease in the strain rate with the steady state being reached $\approx 20\,000$ seconds. The initial increase in the diffusion strain rate is attributed to the significant difference in equilibrium concentration between the bulk and the boundary, based

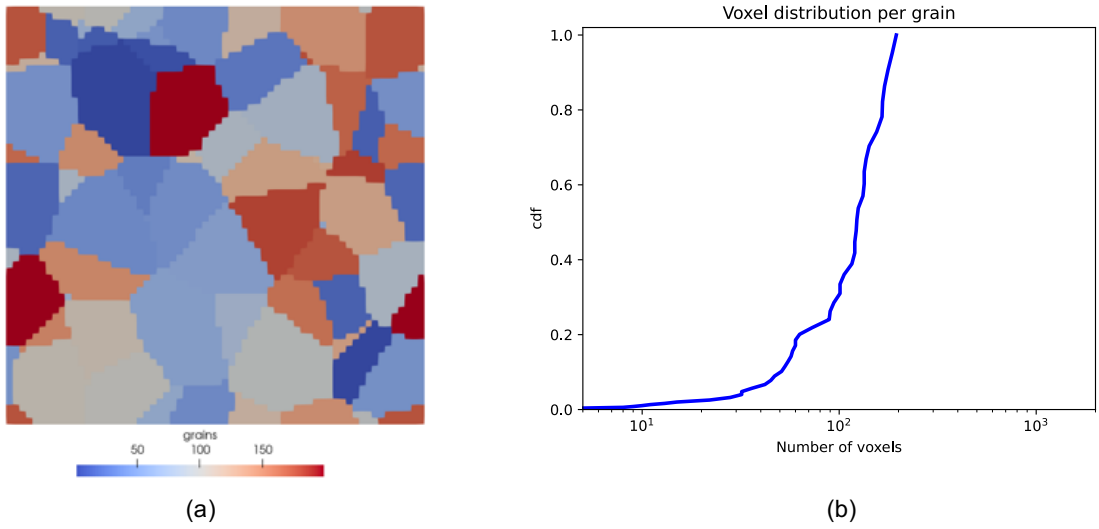


Figure 3.14: Simulation geometry for the full-field simulations consisting of $\approx$ 200 grains with a grid resolution of $64 \times 64 \times 1$, (a). The corresponding average number of voxels per grain distribution is also shown, (b), with each grain having $\approx$ 75 voxels.

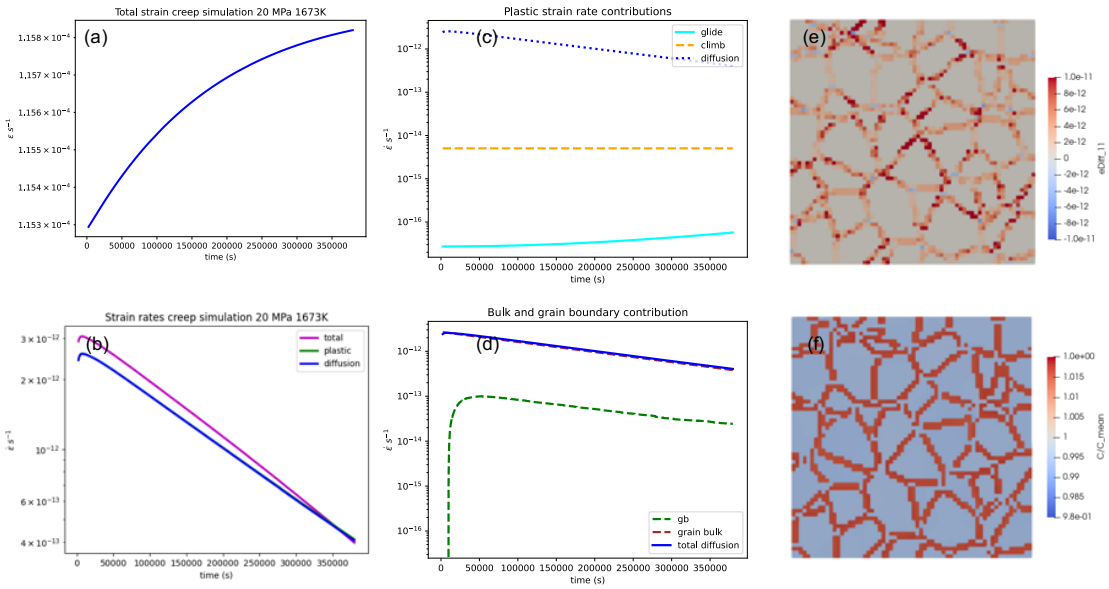


Figure 3.15: Full-field creep simulations of creep in polycrystalline $UO_2$ with 200 grains with an average grain size of $\approx$ 100 µm at 1673 K and 20 MPa creep stress (in the vertical direction). (a) plots the total strain vs. time, while, (b) compares the contribution of the total and diffusion strain rates. Defect diffusion mediated plasticity is the dominant deformation mechanism followed by diffusion climb, while the glide contribution is negligible to the overall plastic deformation, (c). Also, from (d), for this simulation, the dominant diffusion mechanism seems to be that in the bulk. The corresponding distribution of diffusion strain rate, (e), and concentration, (f), is also plotted.

Table 3.4: Material parameters at 1673 K

| parameter | Value | Source | Unit |
|---|---|---|---|
| **Diffusion** | | | |
| $\Omega_0$ | $5.8 \times 10^{-29}$ | [27] | $m^3$ |
| $\delta_{gb}$ | 1.0 | Atomistic simulations | nm |
| $D_0^{gb}$ | 0.000474 | Atomistic simulations | $m^2\,s^{-1}$ |
| $D_0^{bulk}$ | $4.2 \times 10^{-7}$ | Atomistic simulations | $m^2\,s^{-1}$ |
| $E_m^{gb}$ | 2.72 | Atomistic simulations | eV |
| $E_m^{bulk}$ | 4.233 | Atomistic simulations | eV |
| $E_f^{gb}$ | 0.5 | Atomistic simulations | eV |
| $E_f^{bulk}$ | 1.4 | Atomistic simulations | eV |
| $\lambda_{0,bulk}$ | -0.227 | Atomistic simulations | |
| $\lambda_{0,gb}$ | -0.244 | Atomistic simulations | |
| **Climb** | | | |
| $b^s$ | 0.386 | [27] | nm |
| $\rho^s_{cell,edge}$ | 0.1 $\rho^s_{cell}$ | [24] | $m^{-2}$ |
| $Z_v^s$ | 1.0 | [24] | |
| **Glide** | | | |
| $\Delta G_0$ | 7.5 | [28] | eV |
| $\tau_0^s$ | 30.0 | [28] | MPa |
| $\rho^s_{cell}$ | $1 \times 10^{11}$ | This work | $m^{-2}$ |
| $\rho^s_{cellwall}$ | 2.0 $\rho^s_{cell}$ | This work | $m^{-2}$ |
| $p$ | 0.7 | [24] | |
| $q$ | 1.3 | [24] | |
| $n$ | 2.2 | [24] | |
| $\chi_e$ | 1.0 | This work | |
| **Elastic constants at 1673K** | | | |
| $C_{11}$ | 292.306 | [29] | GPa |
| $C_{12}$ | 114.240 | [29] | GPa |
| $C_{44}$ | 56.535 | [29] | GPa |
| $\nu$ | 0.33 | This work | |

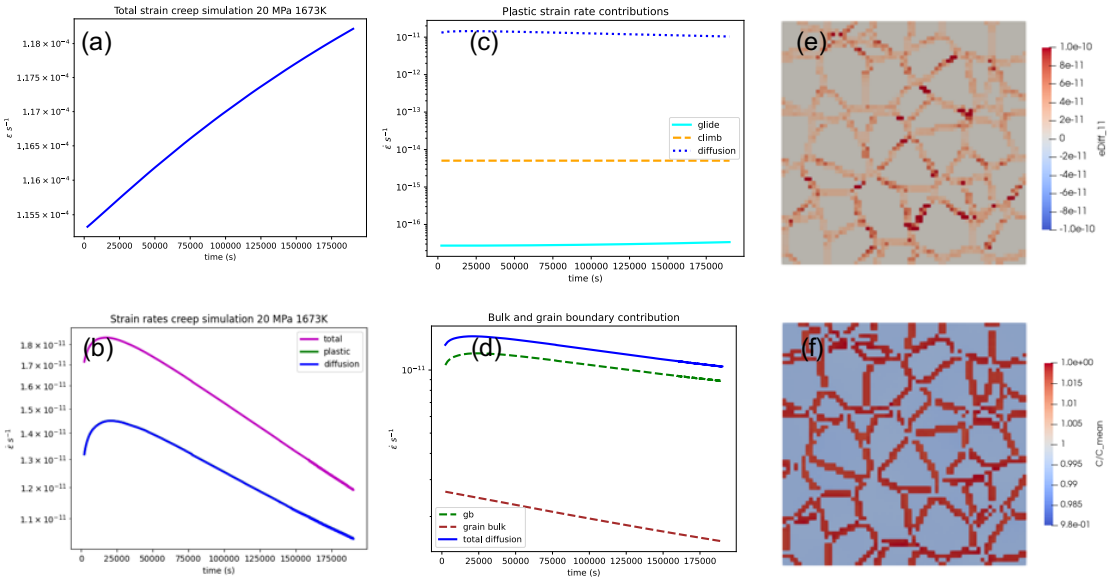


Figure 3.16: Creep simulations with the same microstructure and boundary conditions as in Fig. 3.15, but with a higher negative value of $\lambda_{0,gb} = -0.644$, as compared to $-0.244$. The deformation mechanism is diffusion mediated plasticity, (c), with grain boundary diffusion being the dominating mechanism, (d). Qualitatively, similar concentration profiles as in Fig. 3.15, (f), with high overall diffusion strain rates, (e).

on our assumption of the initial concentration field to be the local equilibrium concentration in the bulk and the boundary. Moreover, diffusion mediated plasticity is the dominant deformation followed by vacancy assisted dislocation climb, with dislocation glide playing negligible role on the overall deformation behavior, Fig. 3.15 (c). Also, for the chosen parameters and grain size, the simulations predict bulk diffusion to be the dominant diffusion mechanism, Fig. 3.15 (d). Furthermore, the uniaxial diffusion strain rate and the concentration fields are also plotted in Fig. 3.15 (e) and (f), respectively. Clearly, there are locations with locally high strain rates, which generally correspond to triple points in the microstructure.

It is important to note that the simulations shown here are preliminary with the steady state values not yet reached.

As mentioned, the model predicts that bulk diffusion is more dominant than diffusion along the grain boundaries, which is different from the analytical predictions. Since, different grain boundaries will have different values, choosing a single value for the entire microstructure may need some level of homogenization of these values. To investigate this influence of the elastic interaction tensor at the grain boundaries, we repeated the polycrystalline creep simulations (at 1673 K and 20 MPa) with a higher negative value of the interaction tensor at the grain boundaries, i.e., $\lambda_{0,gb} = -0.644$ (from the previous case of $-0.244$), with other parameters being same as before, listed in Table 3.4 (the elastic dipole tensor can widely vary depending on the GB type, see previous milestone [6]). Fig. 3.16 plots the results from such simulations with a higher

predicted value of the total strain rate (with a maximum of $\approx 1 \times 10^{-10}\,\mathrm{s}^{-1}$) as compared to the previous simulations (with a maximum of $\approx 1 \times 10^{-11}\,\mathrm{s}^{-1}$). Moreover, with the higher (negative) value of $\lambda_{0,gb}$ the dominant deformation mechanism is predicted to be the GB diffusion, Fig. 3.16 (c) and (d), which also aligns with the expectation from the analytical expressions of creep.

Moreover, observing the concentration and diffusion strain rate distributions in the microstructure, the model also predicts locations with high defect concentration (or high diffusion strain rate), which can also be the sites of failure in the material.

# 4 Discussion and Future Work

This report outlines the development of a creep model for $UO_2$ giving a much improved agreement with the empirical MATPRO correlation and experiment compared to a previous version of the creep model [7]. That being said, this is a difficult problem and there are many improvements that should be addressed to refine this model.

The sensitivity of the GB diffusion coefficient was shown when applied to the Coble creep analytical equation. The acceptable GB diffusion coefficients calculated in this study were only carried out on one GB type. It is important to calculate these values for different GB structures, assess the difference and predict diffusivity values that best describe the variety of different GBs that exist in reality. Moreover, the interstitial defect concentrations at the GB were calculated using a uranium vacancy concentration dependent segregation energy model. Atomistic simulations should be conducted to have a uranium interstitial concentration dependent segregation energy model. Furthermore, due to the relatively high concentration of vacancies and interstitials at the GB under irradiation, annihilation must be occurring. Therefore, there is a need for cluster dynamics simulations to capture these reaction rates, similar to how Centipede does this in the bulk.

In the creep model developed in this study there is a partial pressure dependence. Work should be done to calculate the creep rates not only as a function of temperature and fission rate but also with partial pressure dependence. This is important when comparing to a range of experiments that could have been conducted under different environmental conditions, and to have a working model under differing sets of conditions that can be used in BISON. It is also important for doped $UO_2$ as the dopants can change the oxygen partial pressure [30].

There is the grain size and partial pressure effects that will be accounted for, however, there is also the possibility that Cr doping can occur at grain boundaries impacting the vacancy stability and/or kinetics. Therefore, atomistic calculations should be conducted examining how Cr doped grain boundaries affect the segregation energy models and the mobility of uranium defects.

# 5 Conclusions

This report describes progress in the development of a creep model that is informed using lower-length scale calculations validated against $UO_2$ creep rates, that will be applied to doped $UO_2$. As doped $UO_2$ is an advanced fuel candidate for LWRs, there is a dedicated approach of using multiscale modeling to better understand the performance of this fuel. Doped $UO_2$ has a larger grain size compared to standard $UO_2$, providing better properties. These large grains will also affect diffusional creep and dislocation glide mechanisms. To correctly model creep in doped $UO_2$, it is important to determine the dominant creep mechanism in $UO_2$ as each mechanism will have different grain size dependencies.

In this study, we focus on the development of parameters that impact the Coble creep rate mechanism, namely; diffusion coefficients at the GB and the concentration of defects at the GB. Using a $\Sigma 9$ tilt grain boundary, the uranium vacancy and uranium interstitial diffusion coefficients were calculated. It was found that there was enhanced diffusion, by orders of magnitude, at the GB compared to the bulk. Furthermore, using uranium vacancy concentration dependent segregation energy models developed by Andersson et. al [5], and defect concentrations in bulk $UO_2$ predicted using the cluster dynamics code Centipede, the defect concentration at the grain boundary was predicted at thermal equilibrium and under irradiation. This information was then input into the various creep mechanisms and the creep rates compared to the MATPRO correlation (used in BISON) and experiment. There is an improved match with the available data compared to the previous version of the creep model [7].

Preliminary results have also been generated demonstrating the use of two-dimensional polycrystalline full field simulations informed by lower-length scale atomistic data. From this, the importance of the GB diffusional creep mechanism to overall creep rates was shown. This is a significant step in the use of lower length scale atomistic data capturing the mechanistic behaviour used in the development of a polycrystal plasticity model that can describe $UO_2$ and doped $UO_2$ deformation for in-reactor conditions.

# Acknowledgments

Funding for this work was provided by the US Department of Energy, Office of Nuclear Energy NEAMS (Nuclear Energy Advanced Modeling and Simulation) program. Los Alamos National Laboratory, an affirmative action/equal opportunity employer, is operated by Triad National Security LLC, for the National Nuclear Security Administration of the U.S. Department of Energy under Contract No. 89233218CNA000001.

# References


[1] L. Bourgeois, Ph. Dehaudt, C. Lemaignan, and A. Hammou. Factors governing microstructure development of $Cr_2O_3$-doped $UO_2$ during sintering. *Journal of Nuclear Materials*, 297(3):313–326, 2001.

[2] J. Arborelius, K. Backman, L. Hallstadius, M. Limbäck, J. Nilsson, B. Rebensdorff, G. Zhou, K. Kitano, R. Löfström, and G. Rönnberg. Advanced doped $UO_2$ pellets in lwr applications. *Journal of Nuclear Science and Technology*, 43(9):967–976, 2006.

[3] ANP-10340NP Incorporation of chromia-doped fuel properties in AREVA approved methods.. *Technical report*, April, 2016.

[4] J. D. Hales, S. R. Novascone, G. Pastore, and D. M. Pe. BISON Theory Manual The Equations behind Nuclear F. Technical Report September, Idaho National Laboratory (United States), oct 2013.

[5] D. A. Andersson, S. Vyas, M. R. Tonks, L. Casillas, B. P. Uberuaga, and P. Millett. Simulations of Xe and U diffusion in $UO_2$.

[6] M. W. Cooper and L. Capolungo Demonstrate capability to simulate creep in doped $UO_2$.

[7] K. A. Gamble and M. W. D. Cooper. Multiscale modeling of $Cr_2O_3$-doped $UO_2$ creep and fracture.

[8] F. R. N. Nabarro. Deformation of Crystals by Motion of Single Ions. *Report on a Conference on the Strength of Solids*, 75, 1948.

[9] C. Herring. Diffusional viscosity of a polycrystalline solid. *Journal of Applied Physics*, 21(5):437–445, 1950.

[10] R. L. Coble. A Model for Boundary Diffusion Controlled Creep in Polycrystalline Materials. *Journal of Applied Physics*, 34(6):1679–1682, 1963.

[11] C. Matthews, R. Perriot, M. W. D. Cooper, C. R. Stanek, and D. A. Andersson. Cluster dynamics simulation of uranium self-diffusion during irradiation in $UO_2$. *Journal of Nuclear Materials*, 527:151787, 2019.

[12] A. C. S Sabioni, W. B. Ferraz, and F. Millot. First study of uranium self-diffusion in $UO_2$ by sims. *Journal of Nuclear Materials*, 257(2):180–184, 1998.

[13] S. Plimpton. Fast Parallel Algorithms for Short-Range Molecular Dynamics, 1995.

[14] M. W. D. Cooper, S. C. Middleburgh, and R. W. Grimes. Vacancy mediated cation migration in uranium dioxide: The influence of cluster configuration. *Solid State Ionics*, 266:68–72, nov 2014.

[15] M. S. Daw and M. I. Baskes. Embedded-atom method: Derivation and application to impurities, surfaces, and other defects in metals. *Physical Review B*, 29(12):6443, 1984.

[16] F. A. Kröger and H. J. Vink. Relations between the Concentrations of Imperfections in Crystalline Solids. In *Solid State Physics - Advances in Research and Applications*, volume 3, pages 307–435. 1956.

[17] A. Stukowski. Visualization and analysis of atomistic simulation data with OVITO-the Open Visualization Tool. *Modellind and Simulation in Materials Science and Engineering*, 18(1), JAN 2010.

[18] D. A. Andersson, M. R. Tonks, L. Casillas, S. Vyas, P. Nerikar, B. P. Uberuaga, and C. R. Stanek. Multiscale simulation of xenon diffusion and grain boundary segregation in uo2. *Journal of Nuclear Materials*, 462:15–25, 2015.

[19] R. A. Wolfe and S. F Kaufman. Mechanical properties of oxide fuels (lsbr/lwb development program).

[20] T. E. Chung and T. J. Davies. The low-stress creep of fine-grain uranium dioxide. *Acta Metallurgica*, 27(4):627–635, apr 1979.

[21] E. Clouet, C. Varvenne, and T. Jourdan. Elastic modeling of point-defects and their interaction. *Computational Materials Science*, 147:49–63, 2018.

[22] A. Villani, E. P. Busso, and S. Forest. Field theory and diffusion creep predictions in polycrystalline aggregates. *Modelling and Simulation in Materials Science and Engineering*, 23(5):0–24, 2015.

[23] S. D. Mesarovic. Lattice continuum and diffusional creep. *Proceedings of the Royal Society A: Mathematical, Physical and Engineering Sciences*, 472(2188), apr 2016.

[24] W. Wen, A. Kohnert, M. Arul Kumar, L. Capolungo, and C. N. Tomé. Mechanism-based modeling of thermal and irradiation creep behavior: An application to ferritic/martensitic HT9 steel. *International Journal of Plasticity*, 126:102633, mar 2020.

[25] T. Okita and W. G. Wolfer. A critical test of the classical rate theory for void swelling. *Journal of Nuclear Materials*, 327(2-3):130–139, may 2004.

[26] A. A. Kohnert, B. D. Wirth, and L. Capolungo. Modeling microstructural evolution in irradiated materials with cluster dynamics methods: A review. *Computational Materials Science*, 149:442–459, jun 2018.

[27] H. J. Frost and M. F. Ashby. Deformation-Mechanism Maps for Pure Iron, Two Austenitic Stainless Steels, and a Low-Alloy Ferritic Steel. In *Fundamental Aspects of Structural Alloy Design*, pages 27–65. Springer US, 1977.

[28] T. Tachibana, H. Furuya, and M. Koizumi. Dependence on strain rate and temperature shown by yield stress of uranium dioxide. *Journal of Nuclear Science and Technology*, 13(9):497–502, 1976.

[29] M. T. Hutchings. High-temperature studies of $UO_2$ and $ThO_2$ using neutron scattering techniques. *J. Chem. Soc., Faraday Trans. 2*, 83:1083–1103, 1987.

[30] M. W. D Cooper, G. Pastore, Y. Che, C. Matthews, A. Forslund, C. R. Stanek, K. Shirvan, T. Tverberg, K. A. Gamble, B. Mays, and D. A Andersson. Fission gas diffusion and release for $Cr_2O_3$-doped $UO_2$: From the atomic to the engineering scale. *Journal of Nuclear Materials*, 545:152590, 2021.